JGR Oceans

RESEARCH ARTICLE
10.1029/2021JC017211

Progression of Wave Breaker Types on a Plane Impermeable Slope, Depending on Experimental Design

M. V. Moragues[1] and **M. Á. Losada**[1]

[1]Andalusian Institute for Earth System Research, University of Granada, Granada, Spain

Key Points:

- The progression of breaker types depends on the slope and the wave characteristics at the toe of the slope. It is predictable
- There is a functional relationship between the sets of the relative water depth and wave steepness and of breaker types
- A dimensionless bulk dissipation coefficient is defined which depends on the breaker type and on the relative water depth and wave steepness

Supporting Information:

Supporting Information may be found in the online version of this article.

Correspondence to::

M. V. Moragues,
mvmoragues@ugr.es

Citation:

Moragues, M. V., & Losada, M. Á. (2021). Progression of wave breaker types on a plane impermeable slope, depending on experimental design. *Journal of Geophysical Research: Oceans*, *126*, e2021JC017211. https://doi.org/10.1029/2021JC017211

Received 27 JAN 2021
Accepted 6 APR 2021

Abstract The objective of this research was to analyze the progression of breaker types on plane impermeable slopes. This study used dimensional analysis to demonstrate the relative water depth is a key explanatory quantity. The dominant breaker types depend on the incident wave characteristics at the foot of the slope. Accordingly, it is possible to combine values of H, T, and m. The physical experiments of Galvin, recent numerical results, and new experiments, performed on an impermeable 1:10 slope, were used to verify the result. It was thus possible to obtain the progression of breaker types in different sequences of pairs of combined wave H and T values. Once a sequence is defined, the expected progression of breaker types is predictable, and is well approximated by the log-transform of the alternate similarity parameter. Since the classification of breaker types is discontinuous, the data assigned to each type were placed in horizontal lines, based on the value of log(χ). Given that the breaking of a wave train on a slope should be considered a continuous process, the location of some data was corrected to satisfy this assumption. There is thus a functional relationship between the sets of the experimental space and of the breaker types. This research also derives the non-dimensional energy dissipation on the slope, considering the wave-reflected energy flux on the slope. It is proportional to a dimensionless bulk dissipation coefficient which depends on the breaker type and, therefore, on the value of χ at the toe of the slope.

Plain Language Summary The main objective of this research was to analyze the progression of breaker types on a plane impermeable slope. This study used dimensional analysis to demonstrate that the relative water depth is a key explanatory quantity. The dominant breaker types depend on the incident wave characteristics at the foot of the slope, h/L, and H/L, and also on the slope, m. Accordingly, different combinations of these three parameters can be made. Data from different data sets performed on an impermeable slope with a 1:10 slope angle were used to verify that result. After several analyses of different experimental techniques, it can be concluded that there is a functional relationship between the sets of the experimental space and the breaker types.

1. Introduction

Plane slopes are the most common type of coastal protection because of their ability to transform incident wave energy by reflection, transmission, and dissipation. They can also be designed and built with different angles, materials, and sizes. Their hydrodynamic performance depends on the kinematic and dynamic regimes that develop while the wave train interacts with the slope. Those regimes are directly related to the type of wave breaker (Battjes, 1974; Díaz-Carrasco et al., 2020).

Iribarren and Nogales (1949) used the Iribarren number or surf similarity parameter (Battjes, 1974), (Ir or ξ), to determine when the predominant mode of wave energy transformation is reflective or dissipative, where $Ir = m / \sqrt{H^* / L^*}$, $m = tan(\alpha)$, and α is the slope angle, and H^* and L^* are the characteristic wave height and wave length, respectively, at a certain location.

Galvin (1968) identified and quantified nine breaker types obtained from films on three laboratory beaches (plane impermeable slope). Neglecting some of the breaker types (6–9 in his Table 3) that were most strongly affected by the experimental conditions (reflected and secondary waves), Galvin's classification includes the following types: spilling (1), weak plunging (3), plunging (2), collapsing (4), and surging (5). The ID numbers are those given by Galvin (1968) in Table 3. His Table 6 shows the transition values between breaker types, Surging-Plunging and Plunging-Spilling, for his inshore and offshore parameters for slopes 1:10

and 1:20. Furthermore, there is a continuous gradation in the type of breaking from spilling to plunging to surging (Galvin, 1968).

Battjes (1974) followed and extended Galvin's work. He assumed that for waves breaking on the slope, the value of the relative depth in front of the slope was not important and that the Reynolds number was usually larger than some minimum value, which did not significantly affect the resultant motion. He thus obtained the following reduced approximated relationship, (see Appendix A for an extended analysis of the main assumptions and their implications),

$$X \approx f\left(\alpha, \frac{H}{L_0}\right) \approx f(\xi) \tag{1}$$

where X is a dimensionless variable (output) for many overall properties of the breaking waves and ξ is a surf similarity parameter, defined by:

$$\xi = \frac{m}{\sqrt{\frac{H}{L_0}}} \tag{2}$$

Recently, Derakhti et al. (2020) investigated the framework for predicting the wave breaking onset for surface gravity waves in an arbitrary water depth. They numerically calculated the progression of regular waves over a plane impermeable beach with different slopes (1:5, 1:10, 1:20, 1:40, 1:100, and 1:200). Except for the slope, 1:200, the relative water depth ($h = 0.5$ m) at the toe of the slope and the wave period ($T_w = 4.0$ s) were constant; $h / L \approx 0.0557$ was also constant. On the 1:200 beach slope, the water depth was $h = 0.3$ m, and $h / L \approx 0.044$. By increasing ξ_0, Derakhti et al. (2020) (their Figures 3a, 3c, 3e, 3g, and 3i), found that there was a progression/transition from spilling to collapsing and surging. In their study, given that ξ_0 was defined by using the wave steepness H_0 / L_0 in deep water, it thus followed that $\xi_0 \neq \xi$.

It should be highlighted that there are different locations where the incident wave characteristics (experimental input) are specified. In Galvin (1968), these were the "hypothetical" deep water wave steepness (offshore parameter) and breaker steepness parameter $\sqrt{H_b / gT^2}$, known as the "inshore parameter", based on quantities measured along the breaker line. Furthermore, in Figures 5 and 6, the classifying parameters used were the offshore parameter divided by the square of the beach slope, and the inshore parameter divided by the beach slope, respectively.

Battjes (1974) used the wave height at the toe of the slope and the deep water wave length, whereas Derakhti et al. (2020) used the deep water wave steepness. In this study, following Baldock and Torres-Freyermuth (2020), Díaz-Carrasco et al. (2020), Hughes (2004), and Moragues et al. (2020), both the incident wave height, H, and the wave length, L, of the regular train is specified at the toe of the slope, where the water depth, h, is constant.

Over the last 25 years, many numerical studies have been published on different breaker types on a smooth impermeable slope (Christensen & Deigaard, 2001; Lara et al., 2008; Gislason et al., 2009; Lakehal & Liovic, 2011; Madsen & Fuhrman, 2008; Ting & Kirby, 1995, 1996; Zhang & Liu, 2008;). The level of detail in these studies makes it possible to identify transitions between the four breaker types proposed by Galvin (1968) and adopted by Battjes (1974). The ones most relevant to this research are the distinction between weak and strong bore (Zhang & Liu, 2008), weak and strong plunging (Lakehal & Liovic, 2011; Ting & Kirby, 1995), and weak bore and surging (Gislason et al., 2009).

Based on those distinctions, Moragues et al. (2020) extended Galvin's classification to six wave breaker types: spilling (1-Sp), weak plunging (2-WPl), strong plunging (3-SPl), strong bore (4-SB), weak bore (5-WB), and surging (6-S). Importantly, the collapsing breaker is split into the strong and weak bore. Galvin´s well developed plunging and plunging are changed to strong and weak plunging, respectively, and his ID numbers are also renamed. Furthermore, they provide a brief description of the transition between consecutive breaker types.

This paper applies the method of dimensional analysis to reduce the number of experimental variables affecting the wave-slope interaction and to improve the scalability of the results. The main objective of this study was to analyze the progression of the extended breaker types on plane impermeable slopes, depending on the experimental design defined by the slope angle and the experimental space defined by the incident wave characteristics, such as relative water depth and wave steepness, $\left(h / L, H_I / L\right)$, as derived from the dimensional analysis (see Appendix A). This research is a natural continuation and logical extension of Battjes (1974), Díaz-Carrasco et al. (2020), Galvin (1968), and Moragues et al. (2020), *inter alia*. A breaker type classification may eventually be useful in coastal protection design against coastal risks such as flooding (Del-Rosal-Salido et al., 2019), the coastal hazard from extreme storms (Grilli et al., 2020), human interaction with large-scale coastal morphological evolution (Baquerizo & Losada, 2008) and uncertainty in the assessment of coastline changes, Kroon et al. (2020), among others.

The rest of this paper is organized as follows. Section 2 verifies Battjes' assumption on the importance of the relative water depth at the structure. The physical experiments of Galvin (1968) and recent numerical results of Derakhti et al. (2020) were used for this purpose. Section 3 presents the experimental design along with the physical (CIAO) and numerical experiments (IH-2VOF) conducted on an impermeable slope 1:10. As explained in Section 4, the results of these experiments were used to delimit the approximate regions of the experimental space defined by $(\log\left(H_I / L\right), \log(h / L))$, where each of the six breaker types most frequently occurs. The extended breaker type classification in Moragues et al. (2020) is used. Section 5 shows the link between the experimental technique and the expected breaker types. Section 6 examines the implications of the transitional intervals of the breaker type classification for its applicability, based on the continuous hypothesis of the breaker progression. Next, in Section 7, the need to define the characteristics of the incident train at the toe of the slope and the approximation of the non-dimensional energy dissipation on the slope, considering the wave-reflected energy flux and the wave breaker type is discussed. Finally, the conclusions derived from this research are presented in Section 8. Appendix A revises the dimensional analysis for the experimental characterization of a regular wave train impinging on a plane impermeable slope. Appendix B describes the tests carried out by (Galvin, 1968) and (Derakhti et al., 2020) and specifies numerical data pertaining to the IH-2VOF model (Lara et al., 2008). It also includes information regarding the physical tests carried out in the CIAO wave flume (Addona et al., 2018; Andersen et al., 2016; Lira-Loarca et al., 2019; Moragues et al., 2020).

2. Verifying Battjes's Assumptions

By applying the method of dimensional analysis (see Appendix A) for a given slope angle, it was possible to obtain a functional relationship between the flow characteristics on a plane impermeable slope and the non-dimensional variables, h / L and H_I / L. The $\pi-$theorem does not provide the form of the functional relationship. This form can only be obtained by physical or numerical experimentation or by theoretically solving the problem (Sonin, 2001). Based on experimental evidence that flow characteristics and breaker types are two facets of the same process, in contrast to Battjes (1974), it was expected that for each slope, $m = \tan\alpha$, there would be a functional relationship between the wave breaker types and the non-dimensional variables, h / L and H_I / L, determined at the toe of the structure.

Galvin's experimental data pertain to three slopes: (a) $m = 1{:}5$; (b) $m = 1{:}10$; and (c) $m = 1{:}20$. For each one, the stroke, S_w, of the generator and the wave period, T varied. Following linear theory (Dean & Dalrymple, 1991), the pair of values $\left(H_I, L\right)$ at the toe of the structure were computed. Figures 1a–1c show Galvin's experimental data for the three slopes and the reported wave breaker type. The experimental space for each slope is approximately defined by:

$$Y \approx \mathrm{A}\, X + \mathrm{B} \tag{3}$$

$$X = \log\left(\frac{H_I}{L}\right)$$

$$Y = \log\left(\frac{h}{L}\right)$$

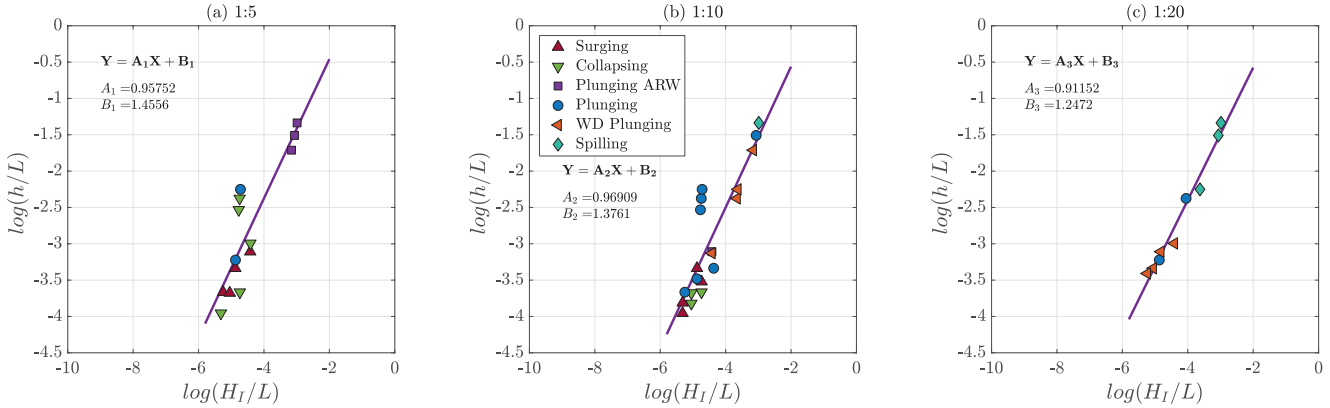

Figure 1. Experimental space (wave input) [$log\left(H_I / L\right)$ versus $log\left(h / L\right)$] and observed output (breaker types) data (Galvin, 1968), for three impermeable smooth slopes: (a) 1:5; (b) 1:10; and (c) 1:20. Breaker types as classified in Table 3 by Galvin (1968). WD plunging and plunging ARW identify well developed plunging and plunging altered by a reflected wave, respectively. For each slope, breaker types evolve with the pair of values, H_I/L, and h/L; The purple line represents the linear fit to the experimental data (Equation 3).

where A and B are the parameters of a straight line fitted to experimental points h / L and H_I / L. It should be highlighted that the approximated linear relationship between the value pairs of the log-transform h / L and H / L determines a very narrow experimental input. The use of the log-transform should help to capture the variability of the experimental output (observed dominant breaker types) under very small changes of the experimental input.

According to Galvin (1968), for each slope (m = *1:5, 1:10,* and *1:20*), the breaker type evolves with the pair of values, H_I / L and h / L. For a given water depth, *h/L*, i.e., $\log\left(h / L\right) \approx -2.4$, the breaker type evolves with the chosen value of m and H_I / L. And for a given wave steepness, H_I / L, i.e., $\log\left(H_I / L\right) \approx -4.8$, the breaker type evolves with the values of m and h / L.

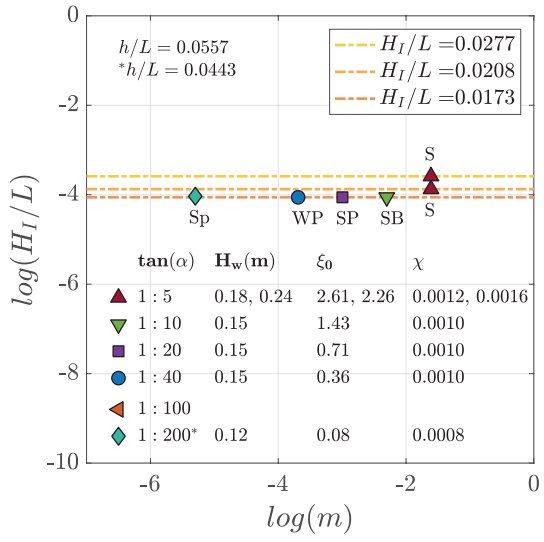

Figure 2. Experimental numerical space input, slope, and H_I/L from Derakhti et al. (2020) under regular wave trains. Data in their Table 1. The relative water depth is constant (h/L ≈ 0.058 except for the 1:200 slope h/L ≈ 0.044). Values of H_w and ξ_0 given by Derakhti et al. (2020) in their Figure 3. $\chi = \left(h / L\right)\left(H_I / L\right)$. The wave height and wave period at the toe of the slope are assumed to be approximately equal to the wave height and wave period at the wavemaker, $H_I \approx H_w$ and $T \approx T_w$.

Figure 2 shows the data of Derakhti et al. (2020) in the numerical experimental space [$log\left(H_I / L\right)$, $log\left(m\right)$] under regular waves, (see their Table 1 "Input parameters for the simulated cases" and the output breaker types in their Figure 3). The value of the incident wave height H_I and of the wave period at the toe of the structure is assumed to be approximately equal to H_w, the wave height, and wave period, $T_w \approx 4$ s, at the wavemaker. Regardless of the value of ξ_0, (equal to the inverse of the square root of Galvin`s offshore parameter), the values of H_I / L and h / L at the toe of the slope are both approximately constant. For a constant water depth *h/L*, that is., h / $L \approx 0.0577$, (0.0443 only for slope 1:200), the breaker type evolves with the chosen value of m and H_I / L. And for a given wave steepness, H_I / L, that is, $\log\left(H_I / L\right) \approx -4.0$, the breaker type evolves with the values of m and the chosen value of *h/L*. Therefore, this dataset for regular waves only confirms that once a pair of characteristic wave values at the toe of the slope is selected and as m progressively decreases, the six breaker types of the classification can be observed.

In summary, the dominant breaker types and their progression/gradation depend on three quantities: (i) the characteristics of the incident waves at the foot of the slope, h / L and H_I / L; and (ii) the slope, m. Obviously, these three can be used to construct a 3D graph, where the prevalence regions of the different breaker types can be observed. However, the interplay of the three quantities is most accurately and usefully represented by graphic representations in a 2D system in terms of value pairs (taken two by two) while the other quantity remains constant.

Table 1
Descriptions of Each Observed Breaker Type, Adapted From Galvin (1968) - his Table 3 - And Moragues et al. (2020) and the Correspondence Between Them

Galvin (1968)	Moragues et al. (2020)
Spilling: Bubbles and turbulent water spill down the face of the wave. The upper of the front face may become vertical before breaking. (ID 1)	Spilling (Sp): The wave volute begins, but disappears in turbulence before it impacts the slope or the wave. The jet evolves at the crest of the wave, above the mean level.
Well-developed plunging: Crest curls over a large air pocket forming a volute. Smooth splash-up usually follows. (ID 2)	Weak plunging (WPl): The wave volute appears and impacts on the wave itself, around the mean level, generating a roller that propagates with the wave.
Plunging: The volute is smaller than in 2. (ID 3)	Strong plunging (SPl): The wave volute appears impacting the slope, hitting it and bouncing back. There is a lot of splashed water and the wave loses a lot of energy. The development of a bump on the leeside of the wave causes the strong jet.
Plunging altered by reflected wave: Small waves reflected from the preceding wave peak up the breaking crest. Breaking otherwise unaffected. (ID 6)	Strong bore (SB): There is an attempt to plunge, but, before it can finish the plunge, the front collapses, generating an inclined plane, mixing water and air bubbles generating a lot of turbulence. The water surface behind the crest is almost plane.
Collapsing: Breaking occurs over lower half of wave. There is no air pocket and no splash-up. There are bubbles and foam. (ID 4)	Weak bore (WB): The inclined plane becomes more vertical, becomes unbalanced, and collapses in the middle or bottom of the water column without volute.
Surging: Wave slides up the slope with little or no bubble production. The water surface remains almost plane except on the beach face during runback. (ID 5)	Surging (S): The wave trains oscillate (like a standing wave), generating no turbulence in the profile. The period of the water rising and falling along the slope is considerably larger than the wave period.

Accordingly, it is either possible to combine values of m and H_I / L, while h / L remains constant, to combine values of m and h / L, while H_I / L remains constant, or to combine values of h / L and H_I / L while m remains constant. In the first option, the data can be plotted based on the surf similarity parameter $\left(\xi = m / \sqrt{H_I / L}\right)$. However, in contrast to Battjes (1974), the dependence of the relative water depth cannot be ignored since for each value of the depth and slope, different sequences of breaker types are obtained. If the wave steepness remains constant and the pairs of h / L and m values are combined, the change in h / L value signifies a change in H (to maintain the wave steepness value), and, consequently, in the progression/transition of breaker types. If m remains constant, the breaker types then depend on the combination of h / L and H_I / L values, Equation 3.

3. Classification of the Wave Breaker Types and Their Expected Variability

Any classification of the breaker types is somewhat subjective and clearly dependent on the observation technique and the experience of the observer. In general, as in Galvin (1968), the experimental information is an ID and a breaker type, based on an overall description of the profile transformation on the slope with emphasis on the steepening and overturning of the wave front and its spatial evolution on the slope. This research used Galvin's classification as extended by Moragues et al. (2020). Table 1 contains both classifications of the breaker types.

Furthermore, seawards of the slope in the water of constant depth, in the transition from a non-breaking wave to a visible breaking process at the crest (Derakhti et al., 2020) might be adopted once the maximum wave steepness at the toe of the slope fulfills Miche's criterion.

$$\left(\frac{H_I}{L}\right)_{max} \gtrsim 0.14 \tanh\left(2\pi \frac{h}{L}\right) \tag{4}$$

As can be observed, this criterion is a crude simplification of the concept of wave breaking, as analyzed in depth by Derakhti et al. (2020). On the other hand, the transition from surging breaker to standing wave (full reflection) might be adopted once overturning at the toe (leading edge) of the wave has ceased to occur (Derakhti et al., 2020) and/or the wave tip on the slope is no longer turbulent (Gislason et al., 2009).

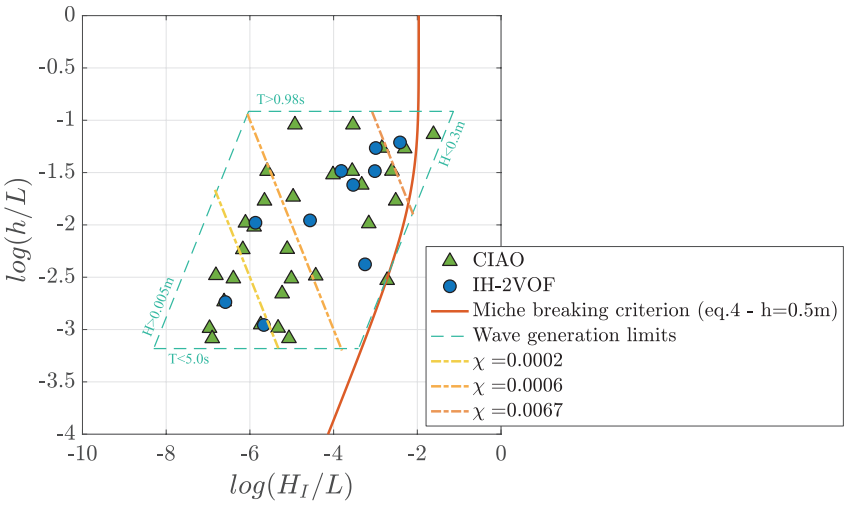

Figure 3. Numerical (IH-2VOF) and physical (CIAO) experimental space, h / L and H_I / L, in a log-transform coordinate system devised for this research study: regular wave train impinging on a plane impermeable slope 1:10. The wave generation limits of the flume are determined by the parallelogram (dashed blue lines). The orange curve shows the maximum wave steepness of a progressive wave train propagating in a constant water depth (h = 0.50 m), as calculated with R. Miche's (1944) equation. Lines of the constant value of $\chi = (h / L)(H_I / L)$ are shown (yellow dashed lines).

3.1. Physical (CIAO) and Numerical (IH-2VOF) Tests and Experimental Design

To determine the dependence of the potential breaker types observed in the wave generation devices, and to delimit the prevalence region of each of the six types, a new set of physical and numerical tests was carried out on a smooth impermeable slope, 1:10.

Numerical tests were performed in the IH-2VOF model (Lara et al., 2008). In this research, a new numerical experimental set-up (ID code IH-2VOF) was implemented. See Moragues et al. (2020) for the set-up and the details of the physical experiments in the Atmosphere-Ocean Interaction Flume (CIAO) wave flume (ID code CIAO). Photographs and video cameras were used to record the breaker types.

Regular wave trains were simulated with a combination of H and T to cover as much area as possible inside the experimental space. To compare physical and numerical results, some tests were run with the same input as in the CIAO flume. For more information about the numerical and physical tests, see Appendix B and supporting information.

The conventional experimental technique (Galvin, 1968; Van Der Meer, 1988) involves building a ramp with a fixed slope, and running sets of tests with a fixed wave period, while progressively increasing the wave height. Since this study involved a ramp with a constant slope (e.g., $m = 1 : 10$), the breaker types depended on the combination of h / L and H_I / L values, Figure 3. The pairs of values were thus selected so as to be able to observe the largest possible number of breaker types and their progression, and also to plot them, according to the wave characteristics and the alternate similarity parameter, χ (Equation 4). Díaz-Carrasco et al., (2020) showed that this provides an accurate description of the interplay between the characteristic wave pairs (h / L, H_I / L) in the wave energy transformation processes on a given slope.

$$\chi = (h / L)(H_I / L) \tag{5}$$

3.2. Observed Predicted Breaker Types and Their Expected Variability

The extended classification of six breaker types (Moragues et al., 2020) is mainly based on the work by Ting and Kirby (1995, 1996) for spilling and weak and strong plunging, Lakehal and Liovic (2011) for strong plunging, Zhang and Liu (2008) for the strong and weak bore, Gislason et al., (2009) for surging, and

Galvin (1968) and Derakhti et al. (2020) for spilling, plunging, collapsing and surging. The numerical and physical model by the authors completes the existing database. It is obvious that the adscription of observation to a breaker type has a subjective component, in particular in the case of the transitions of breaker types

To minimize the subjectivity, in addition to the classical descriptions reflected in Figure 11 of Galvin (1968) and Figure 3 of Derakhti et al. (2020), some distinctive features of each breaker types are used:

- The jet of a weak plunging hits the front slope of the wave around the mean water level, while in the spilling breaker the jet evolves locally at the crest and above the mean water level.
- The jet of a strong plunging breaker hits the water surface or the return flow landwards of the front slope. The existence of a strong jet is related to the development of a hump on the leeside of the crest. This increases the pressure and strengthens the water circulation from the bottom toward the jet, see Figure 1 of Galvin (1968) and Figure 9 of Lakehal and Liovic (2011). Straight "furrows" moving parallel to the crest, and behind it, identifying the sequence of developed vortices with horizontal axes.
- This hump is not observed in a strong bore. The water surface behind the crest is "almost" plane and collapses at different parts of the front above the bottom, see Figure 5 of Zhang and Liu (2008).
- A weak bore develops a turbulent front face and at the toe, a slip thin up-rush layer with a turbulent front, see Figure 1 of Galvin (1968) (collapsing breaker) and Figure 3 of Zhang and Liu (2008).
- Surging breaker is almost an oscillatory motion with a very narrow tip with bubbles, see Figure 1 of Galvin (1968) (surging breaker) and Gislason et al. (2009).

4. Prevalence and Progression of Breaker Types

Figure 4a shows photographs of the six breaker types included in the extended classification. They are similar but not exactly the same as those in Moragues et al. (2020). It is not unusual for one observer to associate the same breaker type in two wave trains, whose progression shows certain differences, and for another observer to consider them to be two different breaker types. Figure 4b shows the photographs of two breaking waves both classified as strong plunging (SPl). The first one is more similar to (or shares characteristics with) a strong bore (SB), whereas the second one is closer to a weak plunging (WPl) breaker. Indeed, the volume of each wave impacts at different points, such as the front slope or the toe of the wave, and both waves show a "hump" on the sea side of the wave crest (a distinct feature of plunging breakers), although of different dimensions. Nevertheless, both breaker types are classified as SPl. Figure 5 shows the location of the photographs in the experimental space.

One cause of these discrepancies, as discussed further on, is that the classification is based on "transitional intervals" of the breaker types, whereas observed reality progresses more gradually. Moreover, thanks to the improvement in visual techniques and advanced numerical codes, it is now possible to obtain very detailed information regarding the progression of the kinematics and dynamics of the breaking process, small-scale behaviors, flow features, and the fluid-air interaction (Derakhti et al., 2020; Zhang & Liu, 2008). For this reason, discrepancies regarding interval classification, visual wave channel observation, and the quasi-continuous description of the numerical models will doubtlessly increase.

4.1. Regions of Prevalent Breaker Type

Based on previous work (Díaz-Carrasco et al., 2020; Moragues et al., 2020) and after the visualization of a large number of photographs, videos, and numerical results, green strips were plotted in the experimental space of the test performed in the CIAO wave flume and with the numerical model IH-2VOF on an impermeable *1:10* slope, Figure 6. Each strip signals the border between contiguous breaker types. They mark the boundaries of the regions in the experimental space where each of the six breaker types is prevalent. Their width merely indicates that at the moment, with the current data set and the intrinsic variability of breaker types, it is difficult to be more precise. It should be highlighted that the strips follow straight lines of the constant value of $\chi = \left(h / L\right)\left(H_I / L\right)$. This configuration of the regions is specific to the slope with $m = 1{:}10$.

For a given relative depth, when $log\left(H_I / L\right)$ is increased, the line parallel to the *x*-axis crosses the strips that separate the prevalence regions of some of the six breaker types of Galvin's extended classification: S, WB, SB, SPl, WPl, and Sp. The blue dashed lines determine the sample space of the value pairs $\left[h / L, H_I / L\right]$

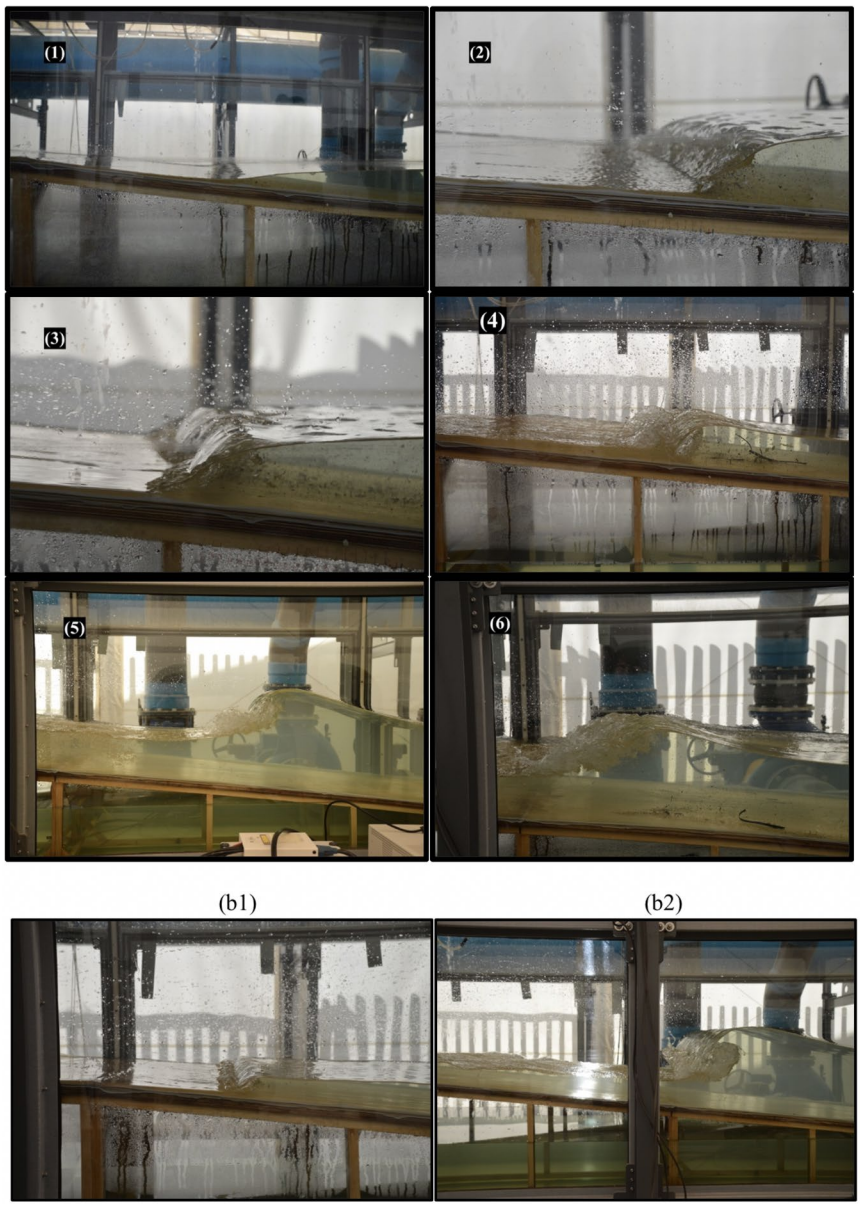

Figure 4. (a) Evolution of breaker types observed in the CIAO wave flume for a 1:10 impermeable slope. ID Numbers (1–6) identify the data in the experimental space. (b) Photographs of (b1) strong plunging closer to a strong bore ($log\left(H_I / L\right) = -4.96, log\left(h / L\right) = -1.73$): volute impacts with the slope generating a vertical wall of water and bubbles, and shows a small "hump" on the sea side of the wave crest. (b2) strong plunging closer to a weak plunging ($log\left(H_I / L\right) = -3.16, log\left(h / L\right) = -1.98$): the upper part of the volute impacts in the lower wave front, and shows a large "hump" on the sea side of the wave crest.

that can be generated in the CIAO flume. For $h / L \approx 0.23$, $\log\left(h / L\right) \approx -1.5$, no wave breaking can be observed in WB and S, and for $h / L \approx 0.05$, $\log\left(h / L\right) \approx -3.0$, no wave breaking can be observed in WPl and Sp. Analogously, for a given wave steepness, when $\log\left(h / L\right)$ decreases from deep water to shallow water, the line parallel to the *y*-axis crosses the strips that separate the prevalence regions of some of the six breaker types. For $H_I / L \approx 0.003$, $\log\left(H_I / L\right) \approx -5.8$, SPl, SB and WB can be observed.

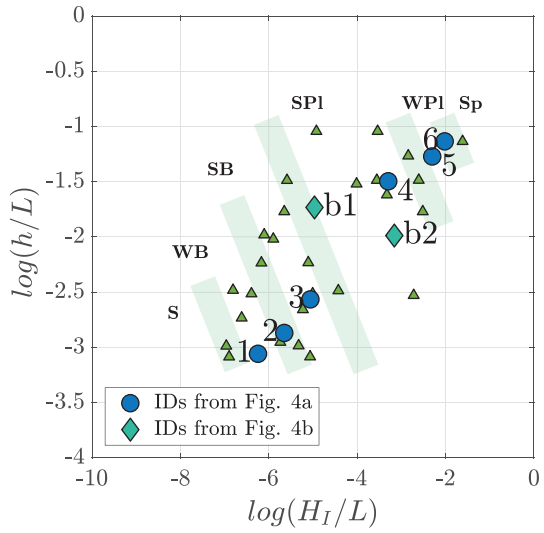

Figure 5. The ID numbers identify the photographs (Figure 4) in the experimental space. (b1) strong plunging closer to a strong bore. (b2) strong plunging closer to a weak plunging. Green strips separate the experimental space in domains where each of the six breaker types prevails: surging (S); weak bore (WB); strong bore (SB); strong plunging (SPl); weak plunging (WPl); and spilling (Sp).

5. The Link Between Experimental Technique, Data Analysis, and Progression of Breaker Types

Figure 7 shows one of the common experimental techniques used in many laboratories for testing hydrodynamic performance on sloping structures. It involves maintaining the Iribarren number or wave steepness constant (in this case, for the same 1:10 slope) in the coordinate system $[log(H_I / L), \log(h / L)]$. Figure 7a shows three vertical lines fitted to three experimental datasets, each with a different wave steepness value. For the same three datasets, Figure 7b shows the corresponding breaker types observed versus the log-transform of the alternate similarity parameter, χ (Equation 4). For each set impinging on a 1:10 slope, only two or three breaker types can be observed.

The white diamonds represent the breaker types observed on some of the sides that delimit the parallelogram of the sample space. The three lines fitted to the three sets of points in Figure 7b correspond to the three vertical lines in Figure 7a, which link the observations to a constant H_I / L. It should be highlighted that in Figure 7a, the points with the same type of wave breaking (e.g., SB and $\log(H_I / L) \approx -5$) are located within their region, whereas in Figure 7b, they are located on a separate horizontal line based on the value of $log(\chi)$. Table 2 shows how the Iribarren number alone is not able to predict the type of breaking as it does not take into account the influence of relative depth. However, the χ parameter takes into account both variables for a given slope angle.

Figures 8a and 8b show the experiments conducted with another common experimental technique, which consists of maintaining the water depth and wave period constant. Thus, when the relative water depth remains the same, and the wave height (or steepness) increases, different breaker types can be observed. In the experimental space $[\log(H_I / L), \log(h / L)]$, Figure 8a shows three lines fitted to three experimental datasets within the parallelogram. Figure 8b shows that for each set impinging on a 1:10 slope at a given relative water depth, three or four breaker types can be observed. As shown in Figure 8a, the points with the same type of wave breaking (e.g., SPl and $\log(h / L) \approx -1.5$) are situated within their region. In Figure 8b, they are located on a horizontal line and are separated, depending on the value of $log(\chi)$.

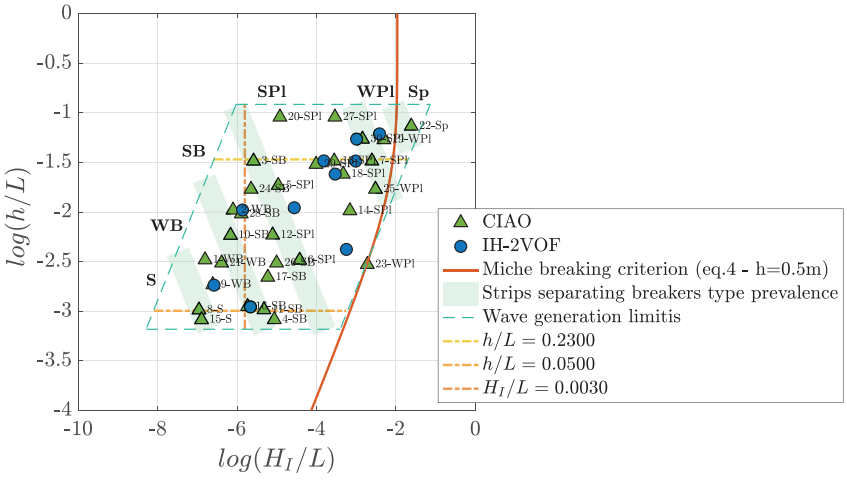

Figure 6. Experimental wave characteristics of the test performed in the CIAO flume and with the numerical model IH-2VOF on an impermeable 1:10 slope. Green strips separate the experimental space in domains where each of the six breaker types prevails: surging (S); weak bore (WB); strong bore (SB); strong plunging (SPl); weak plunging (WPl); and spilling (Sp).

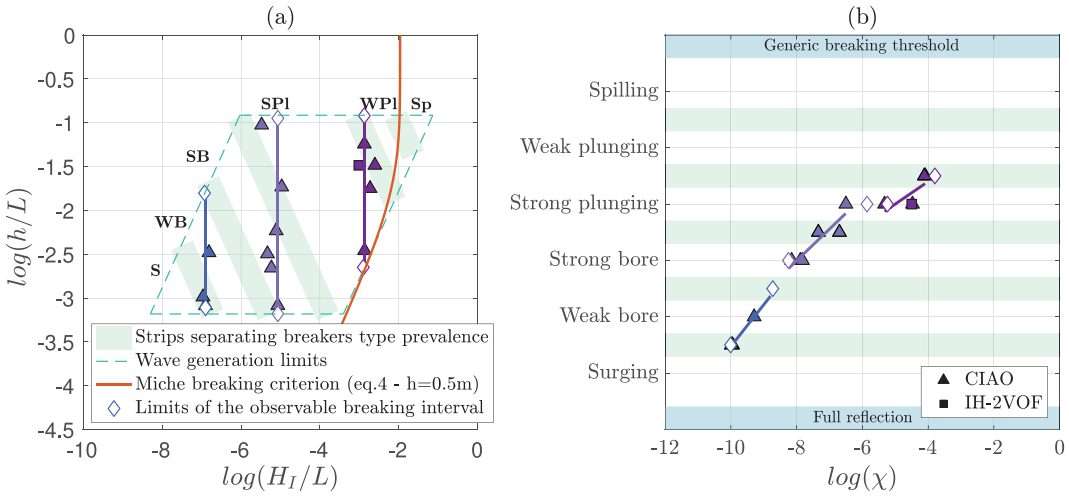

Figure 7. (a) Log-transformed experimental space with a wave steepness limit (Miche's equation) and wave flume generation limits for 1:10 slope. Three lines are fitted to data points following a vertical trend (constant H/L or Ir). (b) Breaker types versus log(χ). White diamonds show the breaker type observed over the sides of the parallelogram experimental space. The fitted straight lines describe the progression of breaker types as a continuous process as a function of χ. Each line corresponds to a fitted line in Figure(a), (with the same color), which satisfies Equation 3.

Figures 9a and 9b shows the experiments in which the water depth remained constant and the wave period and wave height varies. Figure 9a shows three lines fitted to three experimental datasets within the parallelogram. For the three datasets, Figure 9b shows the corresponding breaker types versus the log-transform of the alternate similarity parameter, $\log(\chi)$ (Equation 4). For oblique lines with a positive slope (purple line) and a shallow or intermediate water depth, all of the breaker types were observed. However, as the relative water depth increased (blue line), some of the breaker types did not occur. Moreover, for the oblique lines with a negative slope (green line) following a green strip, only one breaker type (strong bore) was observed. As shown in Figure 9a, points with the same breaker type (e.g., SB) are located within their region, whereas in Figure 9b, they are located on a separate horizontal line, depending on the value of $log(\chi)$.

For purposes of comparison, Figure 10 shows, for the set of experiments conducted by Galvin (1968) over a 1:10 slope (Figure 1b), the corresponding breaker types versus the log-transform of the alternate similarity parameter χ (Equation 4). The breaker types observed by Galvin (1968) are adapted to the classification proposed in Moragues et al. (2020). Moreover, the straight line fitted to the breaker types observed in the CIAO wave flume (blue line in Figure 9b) 1:10 slope is plotted. Thus, the progression of breaker types on a

Table 2
Values of the Iribarren Number, Iribarren Number for Deep Water Conditions, Wave Height, Wavelength, Breaker Types (BT), the Alternate Similarity Parameter, Wave Steepness and Relative Water Depth, for the Middle Fitted Line in Figure 7, From top to bottom

Data point	Ir	Ir_0	H	L	BT	χ	H / L	h / L
1	1.26	2.38	0.0688	10.929	SB	0.000288	0.0063	0.0457
2	1.37	2.11	0.0381	7.128	SB	0.000375	0.0053	0.0701
3	1.44	2.08	0.0293	6.062	SB	0.000399	0.0048	0.0824
4	1.29	1.68	0.0281	4.659	SB-SPl	0.000648	0.0060	0.1073
5	1.20	1.33	0.0196	2.826	SB-SPl	0.001231	0.0069	0.1768
6	1.55	1.56	0.0058	1.395	SPl	0.001498	0.0042	0.3583

Note. The values show that for closer values of Ir (1.20–1.55) two breaker types can be identified. However, by adding the influence of the relative water depth (χ), as dimensional analysis suggests, more information about what is happening is obtained. The values of the fitted vertical line are $H / L = 0.0063$, $h / L = 0.0457$ and $Ir = 1.26$.

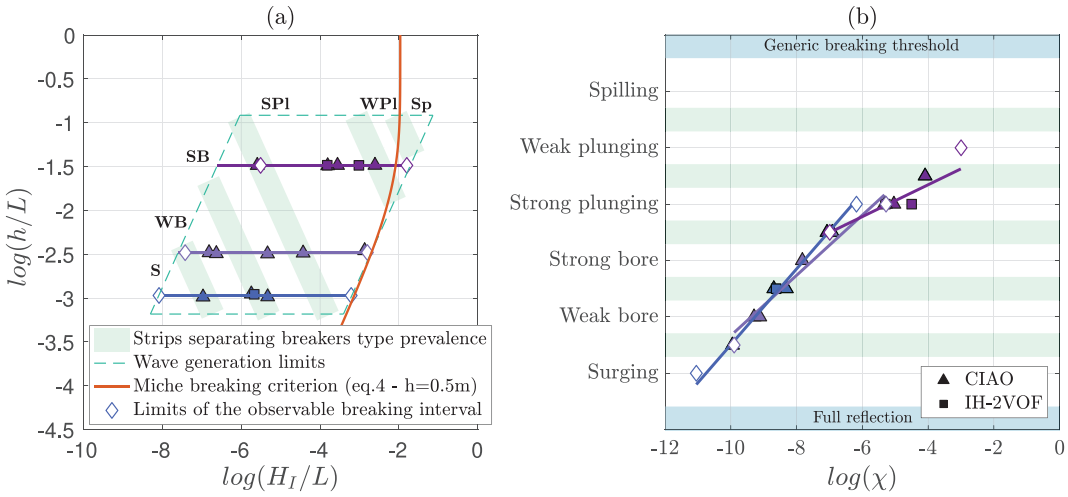

Figure 8. (a) Log-transformed experimental space with a wave steepness limit (Miche's equation) and wave flume generation limits for 1:10 slope. Three lines are fitted to data points following a horizontal trend (constant h/L). (b) Breaker types versus log(χ). White diamonds show the breaker type observed over the sides of the parallelogram experimental space. The fitted straight lines describe the progression of breaker types as a continuous process as a function of χ. Each line corresponds to a fitted line in Figure(a), (with the same color), which satisfies Equation 3.

given slope depends on the experimental design and technique, and depends on the interplay of the wave characteristics as described by the alternate similarity parameter, χ.

The link between experimental design and technique, data analysis, and progression of breaker types, is also present when the values of m and H_I / L are combined and h / L remain constant. Thus, for a given relative water depth, the progression of breaker types depends on the interplay of the slope and wave steepness, see Figure 2 with the data by Derakhti et al. (2020). Battjes (1974) proposed the use of the surf similarity parameter $\left(\xi = m / \sqrt{H_I / L_0}\right)$. Although the "theoretical" $\xi_0 \neq \xi$ varies, the wave steepness at the toe of the slope, when compared with m, does not vary excessively and ξ mimics m.

Figure 11 shows the observed breaker types, adapted to the classification in Moragues et al. (2020) versus the log-transform of m. Regardless of the fact that the observed dataset is obtained by varying the slope two orders of magnitude, the fitted straight line connecting the data with $\chi \approx 0.001$, describes the progression of breaker types as a continuous process, depending on log(m). Because those data all have the same relative water depth value, the progression of breaker types depends on the interplay of the slope and wave steepness.

6. The Transitional Intervals and the Continuous Hypothesis of Breaker Type Progression

A careful analysis of the photographs (Figure 4b) reveals that the overturn and plunge of the front jet are slightly different. More specifically, they are stronger and larger for $log(\chi) \approx -6.75$, approaching a strong bore, whereas they are weaker and smaller for $log(\chi) \approx -5$, approaching a weak plunging breaker. However, once the observation is ascribed to a breaker type, its vertical position is determined, and all the observations ascribed to the same breaker type, are located on the corresponding horizontal line. The value of $log(\chi)$ determines their ubication on the x-axes and furthermore the separation between them. The resulting plot is the consequence that the classification is based on "transitional intervals" of the breaker types, whereas observed reality progresses more gradually.

The straight lines fitted to the observed breaker types (i.e., Figures 7b, 8b, and 9b) are assumed to be the geometric locus of the continuous process triggered by the corresponding set of experimental input (i.e., Figures 7a, 8a, and 9a). Therefore, to fulfill the continuous hypothesis, the observed breaker types of each

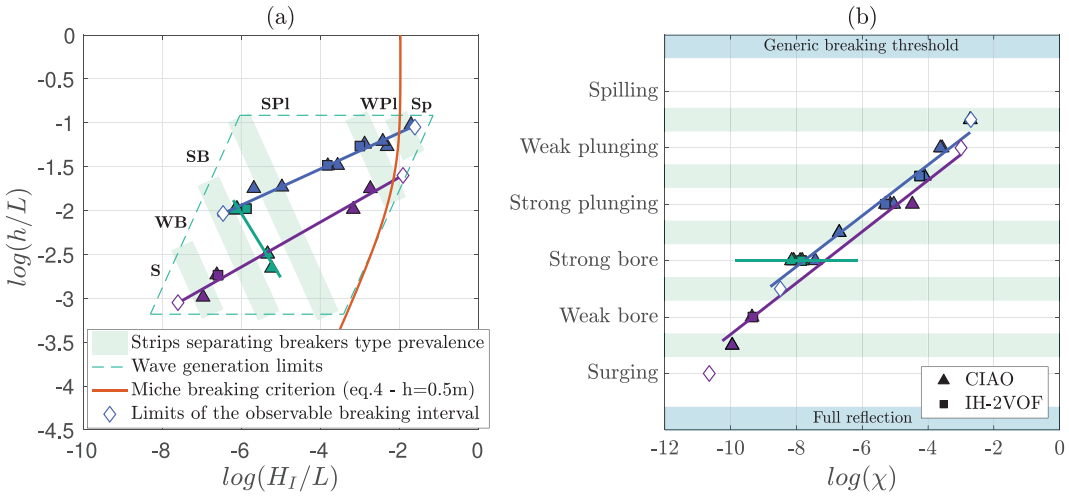

Figure 9. (a) Log-transformed experimental space with a wave steepness limit (Miche's equation) and wave flume generation limits for the 1:10 slope. Three lines are fitted to data points following an oblique trend, Equation 3: two with a positive slope (purple and blue lines) and one with a negative slope (green line). (b) Breaker types versus log(χ). White diamonds show the breaker type observed on the sides of the parallelogram experimental space. The fitted straight lines describe the progression of breaker types as a continuous process as a function of χ. Each line corresponds to a fitted line in Figure(a), (with the same color), which satisfies Equation 3.

dataset (i.e., blue line in Figure 9a) should be on a straight line, (i.e., blue line in Figure 9b). The position of each datum on the *x*-axis should not change, as determined by $log(\chi) = log[h\ /\ LH_I\ /\ L]$.

Figure 12a shows the observed breaker types (blue line in Figure 9b), displaced up or down depending on their $log(\chi)$ value to locate them on the straight line. Analogously, Figure 12b shows the breaker types observed by Galvin on a 1:10 slope (blue line in Figure 10), moved up or down, depending on their $log(\chi)$ value to locate them on the straight line.

In summary, for a given slope, there is a functional relationship between the fitted line in the experimental space (i.e., Figures 1a and 9a) and the straight line determining the progression of breaker types in the function of $log(\chi)$, Figures 12a and 12b.

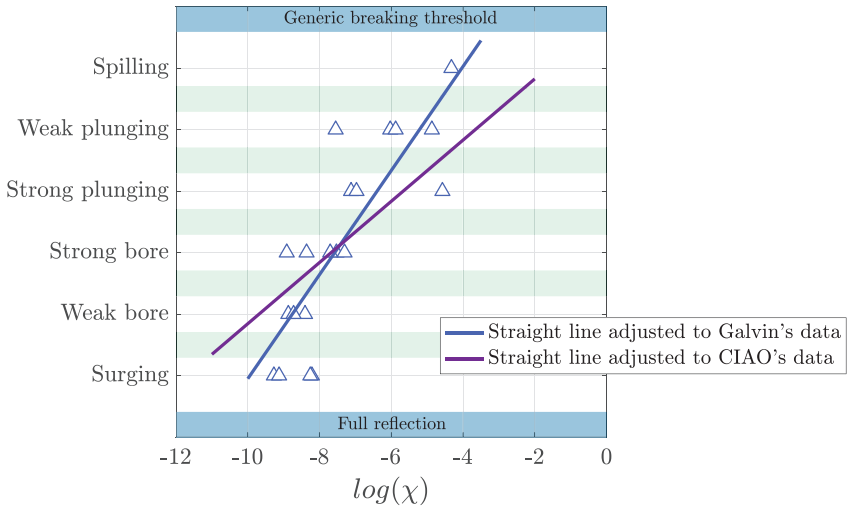

Figure 10. Specific breaker types from Galvin (1968) for 1:10 slope adapted by Moragues et al. (2020) – (S=S, WB = collapsing, SB = plunging ARW and plunging, SPl = plunging, WPl = WD plunging and Sp = Sp) and the fitted straight line to the data (see Figure 1b). For comparison, the fitted straight line (see Figure 9b) to the CIAO data is included.

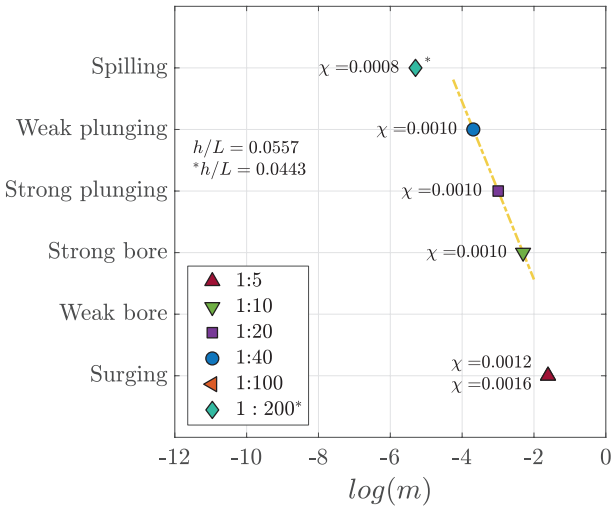

Figure 11. Breaker types from Derakhti et al. (2020) adapted to Moragues et al. (2020). The values of χ are given next to each point. The yellow line connects the three data with a constant value of χ.

7. Discussion

This paper presents a physical and numerical data set of observed wave breaker types over a plane impermeable slope under a regular wave. These data are used to determine the progression of breaker types under different relationships of h / L and H_I / L at the toe of the slope. This study derives the non-dimensional energy dissipation on the slope, considering the wave reflected energy flux on the slope and the breaker type. This energy dissipation is parametrized following Duncan (1981) and Martins et al. (2018), but expressing C, C_g, H_I and T at the toe of the slope.

7.1. Specification of the Input Wave Characteristic at the Toe of the Slope

The characteristics of the incident wave train of experiments by Galvin (1968) and Derakhti et al. (2020) were not given at the toe of the slope. To uniquely specify any of the tests, Galvin chose the following four experimental variables: beach slope, depth at the toe of the beach, generator stroke, and period. For this research, the generated incident wave height was estimated by applying the linear theory of wave generation (Dean & Dalrymple, 1991). In addition, it was assumed that the estimated wave height near the paddle was representative of the incident wave height at the toe of the depth. This implies that the generation of the incident wave was not affected by the reflected wave train, and also that the energy dissipation down at the bed and the side walls of the flume was negligible.

Table 1 of Derakhti et al. (2020) provides the input parameters, namely, the slope and wave height and wave period of the regular wave train at the wavemaker, the distance of the wavemaker to the toe of the slope L_1, and the surf similarity parameter in deep water. For all the simulated cases, P1-r-LV to P6-r-LV, it was considered that $L_1 = 0$. The LES/VOF model specifies the total instantaneous free surface and the liquid velocity at the model upstream boundary. It was then assumed that the incident wave height and wave period at the toe of the structure were approximately equal to their respective values at the wavemaker. Moreover, the output breaker type was taken from Figure 3. Note that this model neglects the interfacial surface tension and viscous stress. Moreover, the subgrid-scale (SGS) stress is estimated using an eddy viscosity assumption and the Dynamic Smagorinsky model, which includes water/bubble interaction effects.

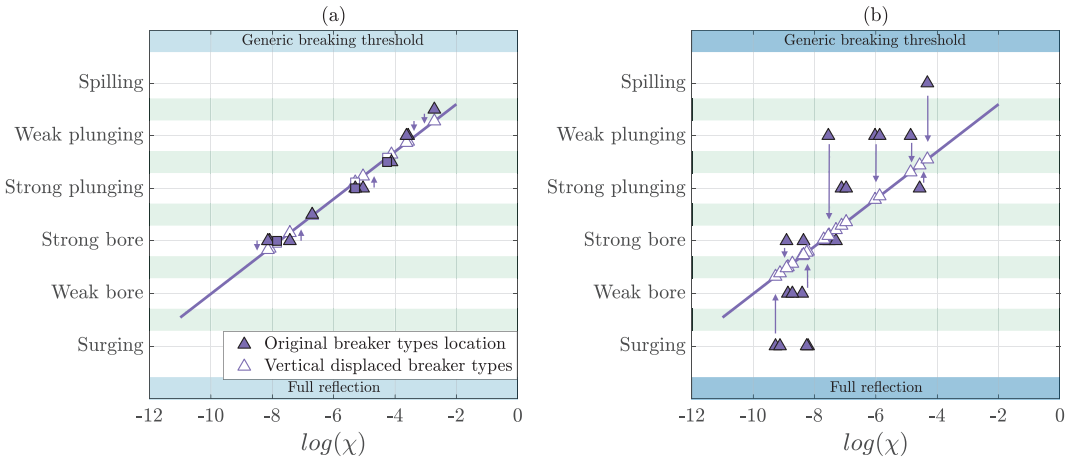

Figure 12. Breaker types versus log(χ) for a 1:10 slope, (a) present data (CIAO flume) from Figure 9b, (b) Galvin's data, 1:10 slope from Figures 1b and 10. The vertical location of the data is modified to fulfill the continuous hypothesis of breaker type progression. For purposes of comparison, breaker types have been adapted to Moragues et al. (2020), based on the original descriptions of the authors.

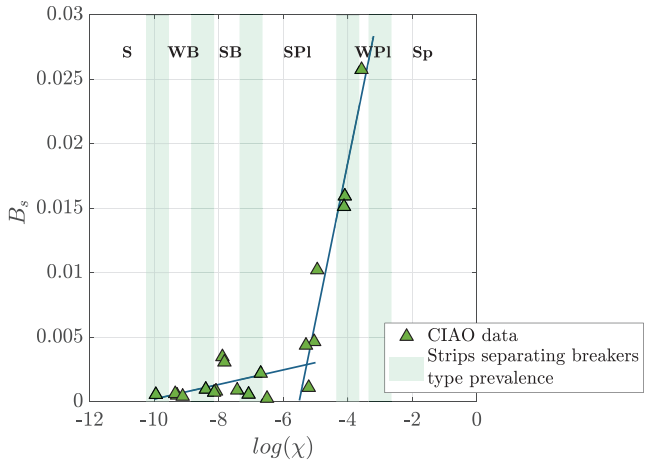

Figure 13. Bulk dissipation coefficient (B_S) vs. $\log(\chi)$ Two lines fitted to the data points show the relation between the coefficient and χ.

The experimental space, depicted in Figures 1 and 2, shows the progression of breaker types under two different conditions, linear relationship $log(H_I / L) - log(h / L)$ (Galvin, 1968), and constant h / L (Derakhti et al., 2020). Independently of the rough method applied to obtain the wave characteristics at the toe of the slope, the breaker types observed by Galvin (1968) and by Derakhti et al. (2020) follow the derived functional relationship.

7.2. Estimated Energy Dissipation for the Observed Wave Breaker Types

The wave energy conservation equation is formulated in a control volume, (CV), extending landwards from the toe of the slope to the shoreline: the spatial variation in the CV of the time-averaged wave energy fluxes is equal to the amount of wave-averaged energy dissipated per unit area, $(D_*)_{CV}, \left(J / \left(m^2 s\right)\right)$, in the CV, (see Baquerizo et al., 1998, for details),

$$\frac{1}{l}\left(\mathcal{F}_I - \mathcal{F}_R\right)_{x_{toe}} + \left(D_*\right)_{CV} = 0 \tag{11}$$

where, $\mathcal{F} = EC_g = ECn = E * \frac{\omega}{k} * f(kh)$, (J/(ms)), is the time-averaged wave energy flux per unit surface at the toe of the slope, x_{toe}, and the subindexes I and R denote the incident and the reflective wave train, respectively. The fluxes in and out at the shoreline, x_{top}, are assumed to be zero; $l = h \cot \alpha$ is the horizontal length of the CV: and h is the water depth at the toe of the slope. Note that all the tests were carried out with the slope $m = 1:10$. Only the energy of the most progressive incident and reflective wave trains were considered. The equation can be expressed in non-dimensional quantities,

$$1 - K_R^2 + d_* = 0 \tag{12}$$

where K_R^2 is the module of the reflection coefficient for the most progressive mode in the wave train, defined as the quotient of the reflected and incident wave energy fluxes per unit surface area, and d_* is the non-dimensional energy dissipation rate,

$$d_* = \frac{\left(D_*\right)_{CV}}{\frac{1}{8}\rho g H_I^2 C_g} l \tag{13}$$

Similarly to the wave breaker type analysis, it is hypothesized that $\left(D_*\right)_{CV}$ can be described as a function of the characteristics of the incident wave train $\frac{h}{L}, \frac{H_I}{L}$ at the toe of the slope. Thus,following Duncan (1981) and Martins et al. (2018), but expressing C, C_g, H_I and T at the toe of the slope,

$$\left(D_*\right)_{CV} \approx B_s \frac{\rho}{g} C^5 \tag{14}$$

$$d_* = B_s \frac{8l}{g^2} \frac{C^5}{H_I^2 C_g} \tag{15}$$

where B_S is a bulk dissipation coefficient. Figure 13 shows the non-dimensional bulk coefficient, B_S versus $log(\chi)$. Depending on the wave breaker types, two regions can be identified. For small values of log ≤ −6, the reflected wave energy flux modulates the wave evolution over the slope. B_s increase slightly as the breaker type progresses from surging to weak and strong bore. For large values of $log(\chi) > -6$, the dissipation by breaking prevails over the reflected energy flux. B_S increases its value as the breaker type progresses from strong bore to strong and weak plunging. Unfortunately, there are not enough numerical data for spilling

breakers but despite this, the slope of the straight line is not expected to change. The equation for d_* can be modified to make explicit the dependence of the wave period, wave steepness, and relative water depth at the toe of the slope.

8. Conclusions

The main objective of this research was to analyze the progression of breaker types on a smooth impermeable slope. This study used dimensional analysis to demonstrate that relative water depth is a key explanatory quantity and that its omission very likely results in an incorrect dimensional analysis model.

The dominant breaker types and their progression/transition depend on three quantities: (i) the characteristics of the incident waves at the foot of the slope, h / L and H_I / L; and (ii) the slope, m. The interplay of these three quantities is most accurately and usefully represented by graphic representations in a 2D system in terms of value pairs (taken two by two) while the other quantity remains constant. Accordingly, it is either possible to combine values of m and H_I / L while h / L remains constant, to combine values of m and h / L while H_I / L remains constant, or to combine values of h / L, and H_I / L while m remains constant.

Dimensional analysis was used to show that the progression of breaker types over the slope, while m remained constant, was determined by a functional relationship of the wave characteristics and the h / L and H_I / L values at the toe of the slope. The experimental input was chosen by combining values of h / L, and H_I / L, and at the same time, by taking into account the experimental design (i.e., the wave generator device and the angle of the slope).

New physical and numerical experiments conducted on an impermeable 1:10 slope were conducted to approximately delimit the regions of the experimental space where each of the six breaker types, as described by Moragues et al. (2020), occurred most frequently. Based on the analysis of four datasets, Galvin (1968), Derakhti et al. (2020), and the present physical and numerical experiments, this research showed that the breaker types on a given slope can be well approximated by the log-transform of the alternate similarity parameter $\chi = \left(h / L\right)\left(H_I / L\right)$.

The progression of breaker types observed inside the experimental space defined by the parallelogram of blue dashed sides was determined by the curve connecting the experimental wave input. In this paper, straight lines, Equation 3, drawn in the experimental space, were used. For each input straight line, there is a corresponding output straight line, which relates the progression of breaker types and $log\left(\chi\right)$. As the wave steepness and relative water depth increase (Figure 7a), there is a continuous gradation in the type of breaking from surging to spilling. The actual observation of breaker types depends on the initial value pairs of h/L and H_I/L selected, the experimental space, and the slope of the straight line (Equation 3). In Table 2, it can be observed that the quality of the breaker type prediction improves significantly when adding the relative water depth. Furthermore, when wave steepness decreases and relative water depth increases but χ remains constant, the breaker type does not change (green line in Figure 7a). In other words, there is no progression of breaker type.

Since the classification of breaker types is discontinuous, the data assigned to each type were placed on horizontal lines, depending on the value of $log\left(\chi\right)$. Because the breaking of a wave train on a smooth slope is assumed to progress continuously, the location of the displaced data was corrected to satisfy that assumption. The line thus obtained establishes, for a given slope (m = 1:10), a linear relationship between the continuous progression of breaker types and the value of $log\left(\chi\right)$. There is a functional relationship between the sets of the experimental space and those of the breaker types. Thus, the breaker types included in the extended classification should be considered as milestones in the continuous wave breaking process on a plane impermeable slope.

The non-dimensional wave energy dissipation on the slope is derived, considering the wave reflected energy flux on the slope. The results show how it is proportional to a dimensionless bulk dissipation coefficient which depends on the breaker type and, therefore, on the value of the alternate similarity parameter χ at the toe of the slope.

Finally, for future research, of wave evolution over a beach or ramp of constant slope m, the experimental design for dimensional analysis should define a complete set of value pairs for h / L and H_I / L, which makes it possible to identify the progression of the observed breaker types. To elucidate the mechanisms which could trigger variations of the wave front it would be convenient to use transversal arrays of gauges that do not perturb the flow (acoustic or similar).

Appendix A: Dimensional Analysis

Battjes (1974) followed and extended the work of Galvin (1968). The assumption is that the motion of periodic, long-crested waves. approaching with normal incidence from deep water or water of a constant depth, h, on a rigid, plane, the impermeable slope is determined by the following set of independent variables: slope angle, α, still-water depth; h, incident wave height; H, at the toe of the slope; wave period, T; acceleration of gravity, g; (dynamic) viscosity, μ; and mass density of the water, ρ. When the wave period is replaced by the deep-water wavelength, L_0, of small-amplitude sinusoidal, long-crested gravity surface waves, then, any dimensionless dependent variable (i.e., flow characteristics run-up, run-down, and possibly, the type of wave breaker or how the wave breaks) depends on seven quantities: $\alpha, h, H, L_0, g, \mu, \rho$.

This is a complete, independent set for the problem, but it is not unique except for the number of variables, $n = 7$. Implicitly, Battjes (1974) used $\left(L_0, g, \rho\right)$ as a complete, dimensionally independent subset, $k = 3$, of the seven independent variables. The dimensions of any of these three cannot be expressed with the dimensions of the other two. Accordingly, the number of independent variables could be reduced from seven to four $\left(n - k = 4\right)$ dimensionless similarity parameters. Battjes (1974) proposed the following four dimensionless independent variables,

$$X = f\left(\alpha, \frac{h}{L_0}, \frac{H}{L_0}, R_e\right) \tag{A1}$$

where Re is a typical Reynolds number, usually larger than some minimum value, above which, any variations in its actual value do not significantly affect the resultant motion. In addition, Battjes (1974) assumed that "for waves breaking on the slope, the value of the relative depth in front of the slope is not important either, this is well established for the relative run-up (Hunt, 1959) and the reflection coefficient (Moraes, 1998) for instance". This results in the following reduced approximated relationship,

$$X \approx f\left(\alpha, \frac{H}{L_0}\right) \tag{A2}$$

And for many overall-properties of the breaking waves, this relationship reduces further to,

$$X \approx f\left(\xi\right); \xi = \frac{\tan\alpha}{\sqrt{\frac{H}{L_0}}} \tag{A3}$$

in which ξ is a similarity parameter.

In the following, the dimensional analysis of Battjes (1974) is revised. Firstly, the set of independent variables governing the problem is modified. The slope angle is a dimensionless quantity and should not be in the complete set of independent variables. The surface tension, τ_s, is included. Next, the input data incident wave height H_I and wave period are characterized at the toe of the slope, as well as the wave length L. Then, X, the type of wave breaker or (how the wave breaks), depends on seven quantities: $h, H, L, g, \mu, \rho, \tau_s$. $\left(L, g, \rho\right)$ is a complete, dimensionally independent subset, $k = 3$, of the seven independent variables. The number of independent variables of the problem is $n - k = 4$,

$$X = \Pi_0 = f\left(\Pi_1, \Pi_2, \Pi_3, \Pi_4\right) = f\left(\frac{h}{L}, \frac{H}{L}, R_e, \frac{\tau_s}{\rho g L^2}\right) \tag{A4}$$

If the motion on the slope is fully turbulent, "the actual value (of $\Pi_3 = Re$) does not significantly affect the resultant motion on the slope" (Battjes, 1974). $\frac{\tau_s}{gL^2}$ is a dimensionless quantity, which indicates the relative importance of surface tension and gravity. It shows up in the surface boundary condition at $z = 0$ (Crapper, 1984). For all the runs carried out in the CIAO flume (see supporting information), this quantity is $O(10^{-6})$. The actual value of Π_4 does not affect the propagation, wave length, and wave celerity of the incident wave trains in the flume.

Since omitting the relative water depth is contrary to the logic that led to Buckingham's π-theorem, then

$$X = \Pi_0 \approx f\left(\frac{h}{L}, \frac{H}{L}\right) \tag{A5}$$

The $\pi-$theorem does not provide the form of the functional relationship expressed by equation (5). Indeed, the form has to be obtained by physical or numerical experimentation, or by solving the problem theoretically. Díaz-Carrasco et al. (2020), Moragues et al. (2020), and this study, based on numerical and experimental data, show that for each slope angle, the interplay of $h\,/\,L$ and $H\,/\,L$, as defined by $\chi = \left(h\,/\,L\right)\left(H\,/\,L\right)$, is a convenient form of the relationship that can be used to explore the type of wave breaker, the flow characteristics, and the transformation of the wave energy on a specific plane slope. Finally, the slope angle of the structure should be regarded as a characteristic of the structure. Consequently, the tests for each slope should be analyzed independently as Galvin (1968) did.

Appendix B: Source and Description of the Data Sets.

1. Galvin (1968)

Galvin (1968) conducted a total of 75 experimental tests at the U.S. Army Coastal Engineering Research Center. He focused on three smooth and impermeable slopes (1:5, 1:10, 1:20) under regular waves. The test conditions are summarized in Table B1. Analyzing a series of 10 consecutive regular waves, a classification of the types of wave breaker was set (i.e., spilling, well developed plunging, plunging, collapsing, surging, and plunging altered by a reflected wave). A clear relationship was found between the onset of wave breaking and the type of breakers and (1) the deep water steepness $\left(H_o\,/\,L_o\right)$ and (2) the "breaker steepness" parameter $\left(\sqrt{H_b\,/\,gT^2}\right)$.

2. Derakhti et al. (2020)

Derakhti et al. (2020) conducted 27 numerical tests (LES/VOF and FNPF-BEM) simulating a planar beach under different wave trains. Regular wave trains were run with a constant wave period and few constant water heights. Six of them have information about the breaker type. Conditions for these six tests are summarized in Table B2.

Table B1
Test Characteristics of Galvin (1968). Parameters H and T are Target values, Namely, the Values Given to the Generation System, and L is the Wave Length and h is the Water Depth

$tan(\alpha)$	$H(m)$	$T(s)$	$h\,/\,L$	$H\,/\,L$
1:5	0.024–0.092	1.00–8.00	0.0191–0.2627	0.0049–0.0505
1:10	0.024–0.109	1.00–8.00	0.0191–0.2627	0.0049–0.0505
1:20	0.054–0.096	1.00–6.00	0.0033–0.2627	1.53–0.0505

Table B2
Test Characteristics of Derakhti et al., (2020). Parameters H and T are Input Values, Namely, the Values Given to the Generation System and L the Wave Length

$tan(\alpha)$	$H(m)$	$T(s)$	h / L	H / L
1:5	0.18, 0.24	4.00, 4.00	0.0577, 0.0577	0.0208, 0.0277
1:10	0.15	4.00	0.0577	0.0173
1:20	0.15	4.00	0.0577	0.0173
1:40	0.15	4.00	0.0577	0.0173
1:200	0.12	4.00	0.0443	0.0177

3. The IH-2VOF Numerical Model

Numerical tests were performed in the IH-2VOF model (Lara et al., 2008). It has a uniform grid on the *y*-axis with a cell size of 5 mm and three regions on the *x*-axis: (a) the generation region with cell size from 8 to 5 mm; (b) the central region (where the slope is located) with a constant cell size of 5 mm; and (c) a third region with cell size from 5 to 10 mm. The total number of cells in the numerical domain is 2993 × 201. All the setups were run with the reflection absorption activated in the generation paddle. Moreover, active wave absorption was used at the generation boundary and at the end of the flume to simulate the dissipation ramp.

The free surface output recorded with 31 wave gauges mostly located along the slope (Figure B1) were used to determine the breaker type. Wave conditions are summarized in Table B3. Using the three gauge method of Baquerizo (1995), the incident wave train and reflected wave train were separated. The zero-upcrossing mean wave height was estimated from the incident ware train.

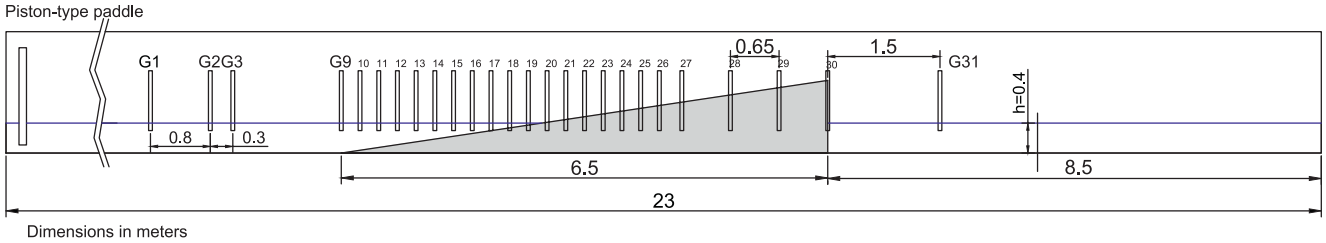

Figure B1. Scheme of the simulated impermeable and non-overtoppable slope in the IH-2VOF and the locations of the 31 wave gauges.

Table B3
Test Characteristics Carried on With IH-2VOF

$tan(\alpha)$	$H(m)$	$T(s)$	$T_z(s)$	h / L	H_I / L
1:10	0.009–0.37	1.1–4.42	1.06–4.417	0.0014–0.297	0.0014–0.0896

Note. Parameters *H* and *T* are input values, namely, the values given to the generation system. *Tz*, *L*, and H_I are the zero-upcrossing mean wave period, wavelength, incident wave height, respectively, obtained from the separation method of incident and reflected wave trains and the statistical analysis of the surface elevation data.

4. The Ciao Wave Flume, University of Granada

The Atmosphere-Ocean Interaction Flume (CIAO) is part of the Environmental Fluid Dynamics Laboratory and focuses on the study of the coupling processes between the sea and the atmosphere. The wave generation system (wave flume), has a width of 1 m, a water depth of 0.70 m, a length of 15 m, and it can generate waves with a period of 1–5 s and a height of up to 25 cm. One of its main features is the presence of two paddles on opposite sides, which are controlled by a software program, for the complete absorption or partial reflection of waves, including a possible phase shift of the reflected wave (Addona et al., 2018; Andersen et al., 2016; Lira-Loarca et al., 2019).

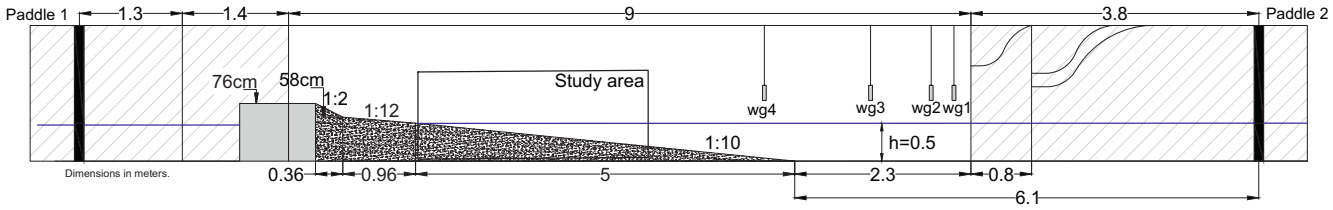

Figure B2. Diagram of the CIAO wave flume and wave gauge position (measured in meters).

Table B4
Test Characteristics Carried on in the CIAO wave Flume

$tan(\alpha)$	$H(m)$	$T(s)$	$T_z(s)$	h / L	H_I / L
1:10	0.005–0.3	0.98–4.8	1.1006–5.0114	0.0457–0.3525	0.0009–0.1990

Note. Parameters H and T are input values, namely, the values given to the generation system. T_z, L, H_I are, the zero-upcrossing mean wave period, wavelength, and incident wave height, respectively.

For this study, an impermeable wooden ramp, with a slope angle of 1:10 (Figure B2) was used. Test conditions are summarized in Table B4. The three-gauge method of A. sunción. Baquerizo (1995) was applied to separate the incident wave train and reflected wave train. The zero-upcrossing mean wave height was estimated from the incident wave train.

5. A Comparison Between Data Sets Used in This Paper

	Galvin (1968)	Derakhti et al. (2020)	IH-2VOF	CIAO
Flume type	Physical	Numerical	Numerical	Physical
Flume dimensions (m) length x wide	29.3 × 0.458	-	23 × 1	15 × 1
Water depth (m)	0.229, 0.305, 0.381, 0.351	0.50, 0.30	0.40	0.50
Generation mode	Piston type	Piston type	Piston type	Piston type
Number of waves	Steady state + 10 waves			At least 50 waves
Seabed angle (before the slope)	0°	0°	0°	0°
Slope angle	1:5, 1:10, 1:20	1:5, 1:10, 1:20, 1:40, 1:100, 1:200	1:10	1:10
Wave type	Regular	Regular	Regular	Regular
Applied wave height in their research	Stroke value	At the wave maker	Incident wave height calculated at the toe of the slope (3 gauges)	Incident wave height calculated at the toe of the slope (3 gauges)
Applied wave height in our research	Wave height at the toe of the slope (calculated first order piston wavemaker solution)	At the toe of the slope: the paddle is at the toe of the slope	Incident wave height calculated at the toe of the slope (3 gauges)	Incident wave height calculated at the toe of the slope (3 gauges)
Wave period in their research and ours	Target value	At the wave maker	Mean wave period calculated	Mean wave period calculated
Observation method for breakers	Filming of 10 successive breaking waves through the grass walls after the generator was operating for 5 min			Pictures and video were taken through the glass walls once the steady state was reached

Data Availability Statement

Readers can access the data in http://doi.org/10.5281/zenodo.4473315.

Acknowledgments
M. V. Moragues was supported by the research group TEP-209 (Junta de Andalucía) and by the following projects: "Protection of coastal urban fronts against global warming–PROTOCOL" (917PTE0538), "Integrated verification of the hydrodynamic and structural behavior of a breakwater and its implications on the investment project–VIVALDI" (BIA2015-65598-P). This work was funded by the projects PCI2019-103565-SUSME and PID2019-107509GB-I00-ROMPEOLAS (SRA (State Research Agency)/10.13039/501100011033). M. A. Losada was partially funded by the emeritus professorship mentoring program of the University of Granada. We would like to thank the three reviewers for providing helpful comments on earlier drafts of the manuscript.

References

Addona, F., Lira Loarca, A., Chiapponi, L., Losada, M. A., & Longo, S. (2018). The Reynolds wave shear stress in partially reflected waves. *Coastal Engineering*, *138*, 220–226. https://doi.org/10.1016/j.coastaleng.2018.04.015

Andersen, T. L., Clavero, M., Frigaard, P., Losada, M., & Puyol, J. I. (2016). A new active absorption system and its performance to linear and non-linear waves. *Coastal Engineering*, *114*, 47–60. https://doi.org/10.1016/j.coastaleng.2016.04.010

Baldock, T. E., & Torres-Freyermuth, A. (2020). Numerical study of the flow structure at a swash tip propagating over a rough bed. *Coastal Engineering*, *161*, 103729. https://doi.org/10.1016/j.coastaleng.2020.103729

Baquerizo, A. (1995). *Reflexión del oleaje en playas: Métodos de evaluación y de predicción*. Universidad de Cantabria.

Baquerizo, A., & Losada, M. A. (2008). Human interaction with large scale coastal morphological evolution. An assessment of the uncertainty. *Coastal Engineering*, *55*(7), 569–580. https://doi.org/10.1016/j.coastaleng.2007.10.004

Baquerizo, A., Losada, M. A., & Smith, J. M. (1998). Wave reflection from beaches: A predictive model. *Journal of Coastal Research*, 291–298.

Battjes, J. A. (1974). Surf similarity. *Coastal Engineering*, 466–480. https://doi.org/10.1061/9780872621138.029

Christensen, E. D., & Deigaard, R. (2001). Large eddy simulation of breaking waves. *Coastal Engineering*, *42*(1), 53–86. https://doi.org/10.1016/S0378-3839(00)00049-1

Crapper, G. D. (1984). *Introduction to water waves*. Ellis Horwood Ltd.

Dean, R. G., & Dalrymple, R. A. (1991). *Water Wave Mechanics for Engineers and Scientists* (Vol. 2). World Scientific Publishing Company.

Del-Rosal-Salido, J., Folgueras, P., Ortega-Sánchez, M., & Losada, M. Á. (2019). Beyond flood probability assessment: An integrated approach for characterizing extreme water levels along transitional environments. *Coastal Engineering*, *152*, 103512. https://doi.org/10.1016/j.coastaleng.2019.103512

Derakhti, M., Kirby, J. T., Banner, M. L., Grilli, S. T., & Thomson, J. (2020). A unified breaking onset criterion for surface gravity water waves in arbitrary depth. *Journal of Geophysical Research: Oceans*, *125*(7), e2019JC015886. https://doi.org/10.1029/2019JC015886

Díaz-Carrasco, P., Moragues, M. V., Clavero, M., & Losada, M. Á. (2020). 2D water-wave interaction with permeable and impermeable slopes: Dimensional analysis and experimental overview. *Coastal Engineering*, *158*, 103682. https://doi.org/10.1016/j.coastaleng.2020.103682

Duncan, J. H. (1981). An experimental investigation of breaking waves produced by a towed hydrofoil. *Proceedings of the Royal Society of London. A. Mathematical and Physical Sciences*, *377*(1770), 331–348.

Galvin, C. J. (1968). Breaker type classification on three laboratory beaches. *Journal of Geophysical Research*, *73*(12), 3651–3659. https://doi.org/10.1029/JB073i012p03651

Gíslason, K., Fredsøe, J., Deigaard, R., & Sumer, B. M. (2009). Flow under standing waves. *Coastal Engineering*, *56*(3), 341–362. https://doi.org/10.1016/j.coastaleng.2008.11.001

Grilli, A. R., Westcott, G., Grilli, S. T., Spaulding, M. L., Shi, F., & Kirby, J. T. (2020). Assessing coastal hazard from extreme storms with a phase resolving wave model: Case study of Narragansett, RI, USA. *Coastal Engineering*, *160*. 103735. https://doi.org/10.1016/j.coastaleng.2020.103735

Hughes, S. A. (2004). Wave momentum flux parameter: A descriptor for nearshore waves. *Coastal Engineering*, *51*(11), 1067–1084. https://doi.org/10.1016/j.coastaleng.2004.07.025

Hunt, I. A. (1959). Design of seawalls and breakwaters. *Journal of Waterway Port, Coastal, and Ocean Engineering Division*, *85*(3), 123–152. https://doi.org/10.1061/jwheau.0000129

Iribarren, C. R., & Nogales, C. (1949). Protection des ports. *XVII, International Navigation Congress, Section II. Comm*, *4*, 27–47.

Kroon, A., Schipper, M. A. de, Gelder, P. H. A. J. M. van, & Aarninkhof, S. G. J. (2020). Ranking uncertainty: Wave climate variability versus model uncertainty in probabilistic assessment of coastline change. *Coastal Engineering*, *158*, 103673. https://doi.org/10.1016/j.coastaleng.2020.103673

Lakehal, D., & Liovic, P. (2011). Turbulence structure and interaction with steep breaking waves. *Journal of Fluid Mechanics*, *674*, 522–577. https://doi.org/10.1017/jfm.2011.3

Lara, J. L., Losada, I. J., & Guanche, R. (2008). Wave interaction with low-mound breakwaters using a RANS model. *Ocean Engineering*, *35*(13), 1388–1400. https://doi.org/10.1016/j.oceaneng.2008.05.006

Lira-Loarca, A., Baquerizo, A., & Longo, S. (2019). Interaction of swell and sea waves with partially reflective structures for possible engineering applications. *Journal of Marine Sciences and Engineering*, *7*(2), 31. https://doi.org/10.3390/jmse7020031

Madsen, P. A., & Fuhrman, D. R. (2008). Run-up of tsunamis and long waves in terms of surf-similarity. *Coastal Engineering*, *55*(3), 209–223. https://doi.org/10.1016/j.coastaleng.2007.09.007

Martins, K., Blenkinsopp, C. E., Deigaard, R., & Power, H. E. (2018). Energy dissipation in the inner surf zone: New insights from Li DAR -based roller geometry measurements. *Journal of Geophysical Research: Oceans*, *123*(5), 3386–3407. https://doi.org/10.1029/2017JC013369

Miche, R. (1944). Mouvements ondulatoirs des mers en profondeur constante on decroissant. *Annals Des Points et Chausses, 1U*, *2*, 25–78.

Moraes, C. de C. (1998). Experiments of Wave Reflexion on Impermeable Slopes. *Proceedings of the 12th International Conference on Coastal Engineering* (Vol. 1 (pp. 509–521). D.C. USA. https://doi.org/10.1061/9780872620285.031

Moragues, M. V., Clavero, M., & Losada, M. Á. (2020). Wave breaker types on a smooth and impermeable 1:10 slope. *Journal of Marine Sciences and Engineering*, *8*(4), 296. https://doi.org/10.3390/jmse8040296

Sonin, A. A. (2001). *The physical basis of dimensional analysis*.

Ting, F. C. K., & Kirby, J. T. (1995). Dynamics of surf-zone turbulence in a strong plunging breaker. *Coastal Engineering*, *24*(3–4), 177–204. https://doi.org/10.1016/0378-3839(94)00036-W

Ting, F. C. K., & Kirby, J. T. (1996). Dynamics of surf-zone turbulence in a spilling breaker. *Coastal Engineering*, *27*(3–4), 131–160. https://doi.org/10.1016/0378-3839(95)00037-2

Van Der Meer, J. W. (1988). *Rock slopes and gravel beaches under wave attack* (PhD). Delft University of Technology.

Zhang, Q., & Liu, P. L.-F. (2008). A numerical study of swash flows generated by bores. *Coastal Engineering*, *55*(12), 1113–1134. https://doi.org/10.1016/j.coastaleng.2008.04.010

References From the Supporting Information

Baquerizo, A., Losada, M. A., & Losada, I. J. (2002). Edge wave scattering by a coastal structure. *Fluid Dynamics Research*, *31*(4), 275–287. https://doi.org/10.1016/S0169-5983(02)00119-3

Baquerizo, A., Losada, M. A., Smith, J. M., & Kobayashi, N. (1997). Cross-shore variation of wave reflection from beaches. *Journal of Waterway, Port, Coastal, and Ocean Engineering*, *123*(5), 274–279. https://doi.org/10.1061/(ASCE)0733-950X

Barthelemy, X., Banner, M. L., Peirson, W. L., Fedele, F., Allis, M., & Dias, F. (2018). On a unified breaking onset threshold for gravity waves in deep and intermediate depth water. *Journal of Fluid Mechanics*, *841*, 463–488. https://doi.org/10.1017/jfm.2018.93

Benjamin, T. B., & Feir, J. E. (1967). The disintegration of wave trains on deep water Part 1. Theory. *Journal of Fluid Mechanics*, *27*(3), 417–430. https://doi.org/10.1017/S002211206700045X

Bowen, A. J., & Inman, D. L. (1969). Rip currents: 2. Laboratory and field observations. 1896-1977. *Journal of Geophysical Research*, *74*(23), 5479–5490. https://doi.org/10.1029/JC074i023p05479

Bruun, P., & Johannesson, P. (1977). Parameters affecting stability of rubble mounds, Closure. ASCE. *Journal of Waterway Port, Coastal, and Ocean Engineering Division*, WW4, 533–566.

Fuchs, H., & Hager, W. H. (2012). Scale effects of impulse wave run-up and run-over. *Journal of Waterway Port, Coastal, and Ocean Engineering Division*, *138*(4), 303–311. https://doi.org/10.1061/(asce)ww.1943-5460.0000138

Guza, R. T., & Inman, D. L. (1975). Edge waves and beach cusps. *Journal of Geophysical Research*, *80*(21), 2997–3012. https://doi.org/10.1029/JC080i021p02997

Kamphuis, J. W. (1975). Friction factor under oscillatory waves. *Journal of Waterway Port, Coastal, and Ocean Engineering Division*, *101*(2), 135–144. https://doi.org/10.1061/awhcar.0000276

Kaneko, A. (1985). Formation of beach cusps in a wave tank. *Coastal Engineering*, *9*(1), 81–98. https://doi.org/10.1016/0378-3839(85)90028-6

Kemp, P. H. (1960). The relationship between wave action and beach profile characteristics. *Coastal Engineering Proceedings*, *1*(7). https://doi.org/10.9753/icce.v7.14

Le Méhauté, B. (1976). *An introduction to hydrodynamics and water waves*. Springer Science & Business Media.

Longuet-Higgins, M. S. (1978). The instabilities of gravity waves of finite amplitude in deep water I. Superharmonics. *Proceedings of the Royal Society of London. A. Mathematical and Physical Sciences*, *360*(1703), 471–488.

Losada, M. A., Roldan, A. J., & Dalrymple, R. A. (1994). Eigenfunction analysis of water wave propagation down a wave flume. *Journal of Hydraulic Research*, *32*(3), 371–385. https://doi.org/10.1080/00221689409498739

McLean, J. W., Ma, Y. C., Martin, D. U., Saffman, P. G., & Yuen, H. C. (1981). Three-dimensional instability of finite-amplitude water waves. *Physical Review Letters*, *46*(13), 817–820. https://doi.org/10.1103/PhysRevLett.46.817

Melville, W. K. (1982). The instability and breaking of deep-water waves. *Journal of Fluid Mechanics*, *115*, 165–185. https://doi.org/10.1017/s0022112082000706

Miche, M. (1951). Le pouvoir réfléchissant des ouvrages maritimes exposés à l'action de la houle. *Annales de Ponts et Chaussées*, *121*, 285–319.

Peregrine, D. H. (1983). Breaking Waves on Beaches. *Annual Review of Fluid Mechanics*, *15*(1), 149–178. https://doi.org/10.1146/annurev.fl.15.010183.001053

Stagonas, D., Warbrick, D., Muller, G., & Magagna, D. (2011). Surface tension effects on energy dissipation by small scale, experimental breaking waves. *Coastal Engineering*, *58*(9), 826–836. https://doi.org/10.1016/j.coastaleng.2011.05.009

Wei, Z., Li, C., Dalrymple, R. A., Derakhti, M., & Katz, J. (2018). Chaos in breaking waves. *Coastal Engineering*, *140*, 272–291. https://doi.org/10.1016/j.coastaleng.2018.08.001